Colloidal-ALD Grown Hybrid Shells Nucleate via a Ligand–Precursor Complex

Ona Segura Lecina[1], Michael A. Hope[2], Amrit Venkatesh[2], Snædís Björgvinsdóttir[2], Kevin Rossi[1], Anna Loiudice[1] Lyndon Emsley[2], Raffaella Buonsanti[1*]

[1]Laboratory of Nanochemistry for Energy, Institute of Chemical Sciences and Engineering, École Polytechnique Fédérale de Lausanne (EPFL), CH-1950 Sion, Switzerland.

[2]Laboratory of Magnetic Resonance, Institute of Chemical Sciences and Engineering, Ecole Polytechnique Fédérale de Lausanne (EPFL), CH-1015 Lausanne, Switzerland.

ABSTRACT

Colloidal atomic layer deposition (c-ALD) enables the growth of hybrid organic/inorganic oxide shells with tunable thickness at the nanometer scale around ligand-functionalized inorganic nanoparticles (NPs). This recently developed method has demonstrated improved stability of NPs and of their dispersions, a key requirement for their application. Nevertheless, the mechanism by which the inorganic shells forms is still unknown, as is the nature of the multiple complex interfaces between the NPs, the organic ligands functionalizing the surface, and the shell. Here, we demonstrate that carboxylate ligands are the key element that enables the synthesis of these core–shell structures. Dynamic nuclear polarization surface enhanced nuclear magnetic resonance spectroscopy (DNP SENS) in combination with density functional theory (DFT) structure calculations show that the addition of the aluminum organometallic precursor forms a ligand–precursor complex that interacts with the NP surface. This ligand–precursor complex is the first step for the nucleation of the shell and enables its further growth.

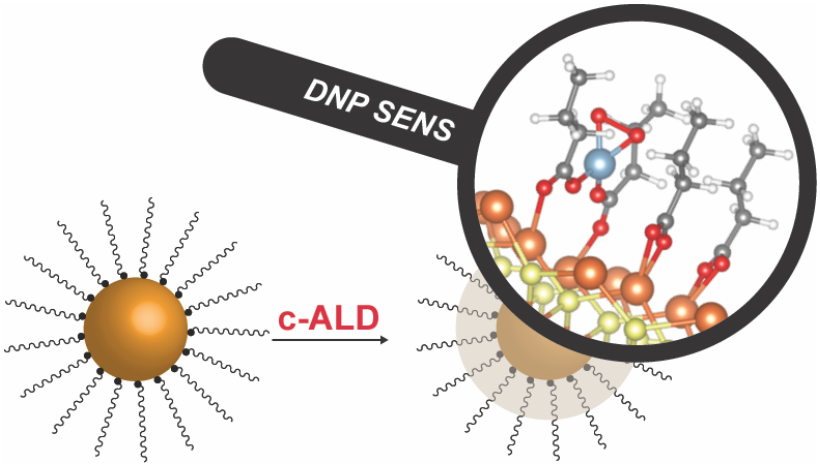

INTRODUCTION

Hybrid organic–inorganic materials are used in a wide range of applications, spanning from energy generation and storage to biomedicine.[1–18] Tuning the composition and structure of both their organic and inorganic components modulates the functional properties which can therefore be optimized for the targeted application.[4,6–14] Furthermore, synergistic interactions at the interfaces can generate unexpected phenomena.[3]

Among different methods for the preparation of organic–inorganic hybrids, sol–gel approaches provide a large degree of freedom in the synthesis of materials that include inorganic clusters in polymeric matrices or organic molecules trapped in inorganic networks.[15–18] For example, hydrolysis/condensation reactions of alkoxide precursors were utilized to embed metal oxide clusters into polysiloxane chains or photoactive molecules inside silica matrices.[15,16] However, the chemistry behind the formation of these materials mostly relies on the particular reactivity of Si-C bonds and silicon alkoxides ($R'_nSi(OR)_{4-n}$), thus it is not trivial to extend it beyond siloxane-based hybrids.[17,18]

Very recently, a solution-based approach, referred to as colloidal atomic layer deposition (c-ALD), was introduced to deposit amorphous oxide shells around nanoparticles (NPs).[19] These NPs are made by colloidal synthesis and thus consist of an inorganic core stabilized by organic capping ligands. The sequential injection of a highly reactive metal precursor and oxygen gas prompts the formation of an amorphous oxide network around the NPs.[19] This methodology enables the growth of a thickness-tunable shell, exemplified by aluminum oxide (AlO_x), and has been demonstrated for different semiconductor NPs (PbS, $CsPbX_3$ with X=Br, I) as well as metallic (Ag) and metal-oxide (CeO_2) NPs. These c-ALD grown core–shell NPs have been used to investigate distance-dependent charge-transfer, and anion-exchange reactions via in-situ X-ray diffraction.[19,20] A recent study demonstrated that the organic surface ligands remain embedded in the AlO_x shell.[21] Thus, these core–shell particles emerge as a novel class of organic–inorganic hybrids with compositional flexibility of the NP core, the oxide network, and the organic ligands.

The c-ALD method holds the promise to expand sol–gel chemistry to a broader compositional range, with a higher level of control at the nanoscale. Knowledge of the mechanisms involved in the hybrid formation is essential to realize this potential. However, due to the compositional and structural complexity of these materials, atomic-level characterization is challenging.

Solution nuclear magnetic resonance (NMR) spectroscopy is among the most common tools to study NP–ligand interactions.[22–30] This technique focuses mainly on the organic species, since

the resolution is often limited by the slow overall tumbling of the NPs. On the other hand, solid-state NMR can provide rich structural and dynamic information for both the core and the capping groups.[31–41] However, NMR experiments are often limited by low sensitivity, especially in the case of NPs with thin shell layers. In recent years, dynamic nuclear polarization surface enhanced NMR spectroscopy (DNP SENS) has been developed to overcome these limitations.[42–48] In these experiments the system is wetted with a solution containing a stable radical, and the greater polarization of the unpaired electrons is transferred to enhance the NMR signal of nuclei at the surface of the material. DNP SENS has been exploited to characterize both the organic and inorganic components of colloidal semiconductor NPs and to discriminate between the NP core and surface atoms.[49–54]

Herein, we elucidate the local structure and bonding in c-ALD grown CdSe@AlO_x core–shell materials by DNP SENS in combination with solution NMR and density functional theory (DFT) structure calculations. We find that the oleate ligands, which cap the surface of the colloidal nanoparticles, provide nucleation sites for the organometallic aluminum precursor, thus enabling the further growth of the shell.

RESULTS AND DISCUSSION

CdSe@AlO_x core–shell hybrids were chosen as a representative model system in order to exploit the previous knowledge on the CdSe quantum dots (QDs) surface chemistry available across the literature.[25,33,51,55–57] Zinc blende CdSe QDs were synthesized following a previously reported procedure with an excess of oleic acid (OLAC) being injected at the end of the synthesis.[58] This ligand binds to the positively charged Cd rich surface to yield oleate-capped QDs.[58] The position of the first excitonic transition in the UV–vis absorption spectrum corresponds to QDs with a diameter of 2.3 nm (**Figure S1**), and the full width at half maximum (FHWM) of 25 nm indicates an ensemble of monodisperse QDs, as depicted in the transmission electron microscopy (TEM) images (**Figure S2**).[59] A ligand density of 5.3 oleate/nm^2 was quantified from the solution ^{1}H NMR spectrum (**Figure S3**), which corresponds to around 85 oleate molecules per QD, in good agreement with the literature.[25,60–62]

The QDs were then coated with an AlO_x shell to obtain the CdSe@AlO_x hybrids, by following the previously developed c-ALD protocol.[19] A typical synthesis is illustrated in **Figure 1.** CdSe QDs are first redispersed in octane, then trimethylaluminum (TMA) is added at a rate of 1 mL/h to the suspension under constant stirring. One c-ALD cycle (n = 1) is completed by bubbling

O_2 gas in the reaction flask (details in the Experimental Section). After 2–3 cycles, additional OLAC is added, instead of O_2, to prevent precipitation of the core–shell structures. These steps can be repeated until the desired shell thickness is achieved.

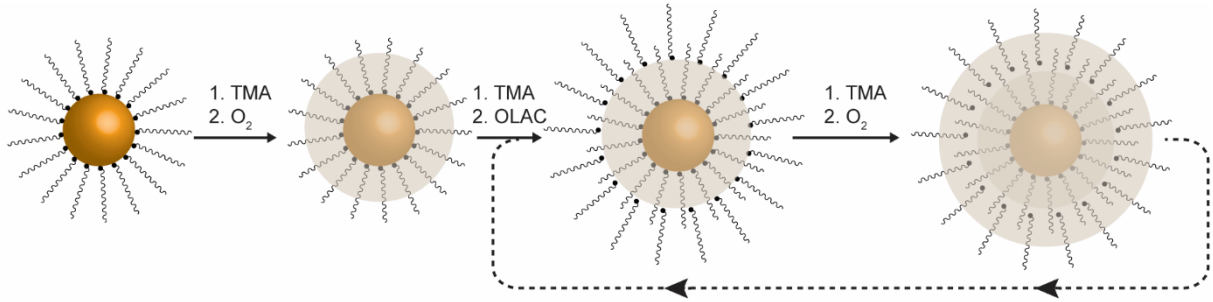

Figure 1. Schematic illustration of the c-ALD process. The first 1 to 3 cycles render a thin shell that can be comparable to a surface treatment of the inorganic cores. Further depositions form a thicker metal-oxide shell which embeds the organic ligands.

Figure 2 reports the characterization of representative CdSe@$AlO_{x(n)}$ samples obtained for different numbers of c-ALD cycles (total n = 3, 5, 10). The UV–vis spectra in **Figure 2a** show that the position and the FWHM of the first excitonic transition remains unchanged between the as-synthesized QDs and those with different alumina shell thicknesses, indicating that neither change in the size nor in the monodispersity of the QDs occurs during the c-ALD. The same samples were analyzed by diffusion ordered NMR spectroscopy (DOSY)[63] (**Figure S4**) to extract the hydrodynamic diameter (d_H), which is reported in **Figure 2b**. The initial d_H of around 3 nm increases to approximately 5 nm after 10 cycles. Because of the small size of the CdSe core and the lack of contrast for amorphous oxides, TEM analysis cannot supply clear information on the shell. However, high-angle annular dark-field scanning transmission electron microscopy (HAADF-STEM) images evidence no change in the morphology of the QDs before and after c-ALD (**Figure 2c,d**), which is consistent with the optical characterization. The different assembly on the TEM grid for CdSe QDs and CdSe@AlO_x provides indirect evidence of a different surface chemistry (**Figure 2c,d**). Additionally, energy-dispersive X-ray (EDX) spectroscopy presents a good spatial correlation between the Se and Al signals (**Figure 2e**), which is clearer when comparing the EDX spectra of the areas with and without CdSe@$AlO_{x(n=10)}$ (**Figure 2f**). Finally, the absence of isolated alumina aggregates confirms that the alumina is deposited only on the QD surface.

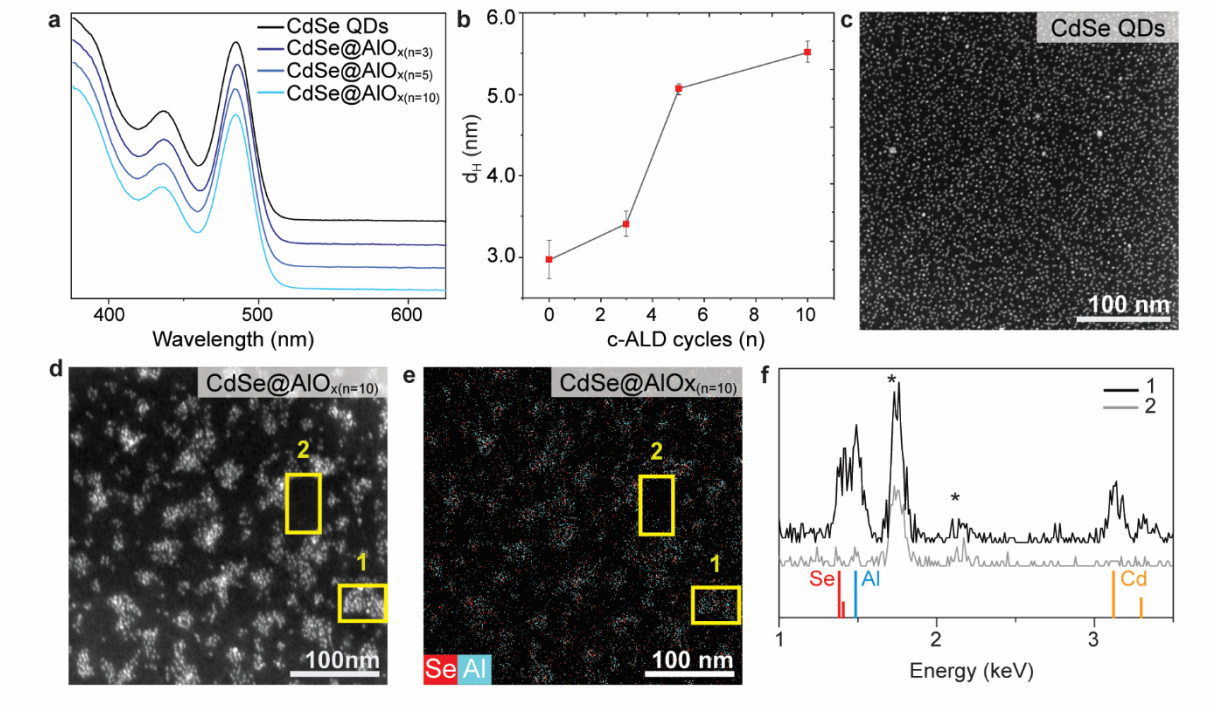

Figure 2. (a) UV–vis absorption spectra of CdSe QDs before (black) and after (blue tones) 3, 5 and 10 cycles of c-ALD. (b) Hydrodynamic diameter of the same samples calculated from DOSY (**Figure S4**). (c,d) HAADF-STEM images of (c) as-synthesized CdSe QDs and (d) CdSe@AlO$_{x(n=10)}$ along with (e) the EDX colored map of CdSe@AlO$_{x(n=10)}$ and (f) spectra of the areas with and without CdSe@AlO$_{x(n=10)}$ in the yellow squares numbered (1) and (2), respectively. Asterisks indicate Si and Au signals arising from the grid.

Surface characterization

X-Ray photoelectron spectroscopy (XPS) and Fourier-transform infrared spectroscopy (FTIR) were performed on CdSe QDs and CdSe@AlO$_{x(n=2)}$ to learn about the effects of alumina nucleation on the surface chemistry. These analyses were carried out on samples obtained for n = 2 to avoid interference from the additional OLAC. XPS shows the presence of two peaks in the Cd 3d region (**Figure 3a**), in both the as-synthesized CdSe QDs and in the core–shell, corresponding to Cd $3d_{3/2}$ and Cd $3d_{5/2}$. Each of these peaks can be fitted with two contributions, positioned at 405.3 and 406.2 eV for Cd $3d_{5/2}$. The low binding energy contribution is assigned to fully coordinated Cd atoms in a core environment, while the high binding energy signal corresponds to under-coordinated Cd atoms at the QD surface, in line with previous reports.[56,64,65] The O 1s region for the CdSe QDs shows only one peak at 531.7 eV corresponding to the oleate species present on the QDs surface as native ligands (**Figure**

S5).[66–68] The absence of cadmium oxide or -OH groups is confirmed by these spectra, consistent with the literature.[69,70]

After the deposition of the alumina shell, a single peak appears in the Al 2s region (119.2 eV), expected for Al-O species. This signal can be correlated to the O 1s spectrum of CdSe@$AlO_{x(n=2)}$, where the peak is fitted at 531.7 and 532.1 eV for C-O and Al-O species, respectively (**Figure S5**). The Cd 3d region does not show significant differences after the deposition of alumina and, remarkably, no Cd-O signals are observed, indicating that the c-ALD protocol does not oxidize the QDs. **Table S1** in the Supporting Information lists the binding energy, area, peak width and assignment of the peaks presented in **Figure 3a** and **Figure S5**.

The FTIR analysis (**Figure 3b**) confirms the presence of alumina in the region between 450 and 750 cm^{-1}, which corresponds to Al-O-Al vibrations. The binding mode of the ligands can be assessed based on the wavenumber difference (Δ) between the asymmetric (ν_{as}) and symmetric (ν_{sym}) stretching modes of the carboxylic/carboxylate moiety, in the region between 1400 and 1700 cm^{-1}. A $\Delta > 250$ cm^{-1} generally indicates a monodentate coordination, as can be observed for free OLAC.[71,72] The difference is narrowed down to ~100 cm^{-1} for both as-synthesized and coated QDs, confirming that native oleate ligands are bound mostly in a chelating configuration.[71,72] However, the asymmetric COO^- stretching band becomes broader at higher wavenumber for CdSe@$AlO_{x(n=2)}$. According to previous reports, this shoulder located at around 1550 cm^{-1} indicates the presence of carboxylates bound in a bridging configuration, with each oxygen coordinating to different metal centers.[71,73] This result points to changes in the ligand binding mode upon nucleation of the alumina. Bands at 722, 2844, 2920 and 3007 cm^{-1} indicate that the alkyl and alkene regions of the ligand chain remain unaltered during the process. Finally, the broad feature in the high-wavenumber region is indicative of -OH groups after the deposition of the AlO_x shell. Based on the XPS results, this feature is attributed to Al-OH.

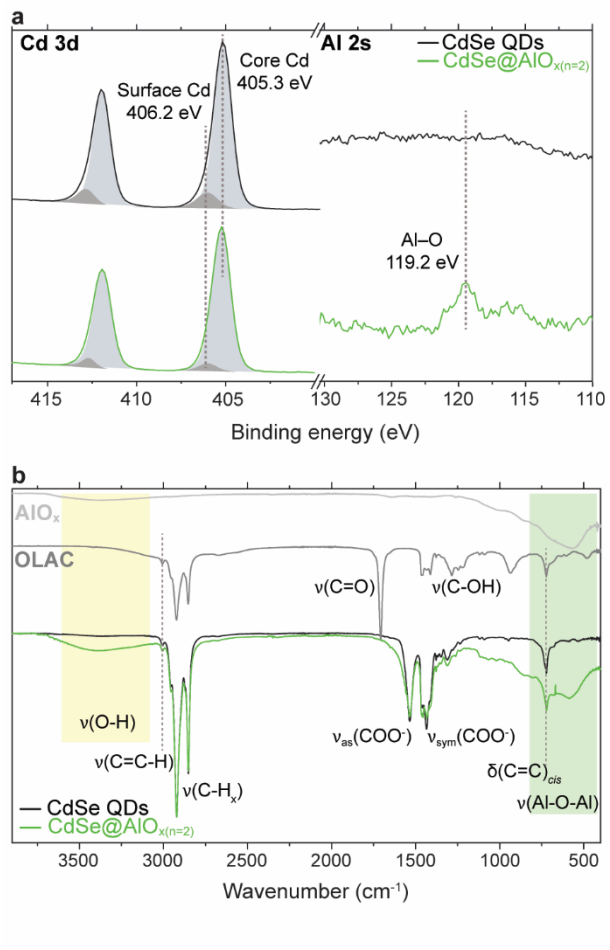

Figure 3. (a) XPS spectra of CdSe QDs (black) and CdSe@$AlO_{x(n=2)}$ (green) for the Cd 3d and Al 2s core-level regions. (b) FTIR spectra of the same samples along with pure OLAC and AlO_x as references. The yellow and green regions highlight the ν(O-H) and ν(Al-O-Al) broad signals, respectively.

Surface titration with TMA monitored by solution NMR

In gas-phase ALD, it is known that oxidized surface species (most generally surface -OH) react with TMA to nucleate the AlO_x layer and anchor it to the substrate.[74,75] The surface analysis discussed above shows that there are no -OH groups on the surface of the CdSe QDs, and that oleate ligands are the only oxygen-containing species present on the as-synthesized QDs. Interaction of the aluminum precursor with the positively charged Cd-rich surface is unlikely.[76] As such, it is reasonable to hypothesize that the oleate ligands interact with the TMA and are involved in the nucleation of the shell.

To investigate the changes to the CdSe QDs and the ligands on addition of TMA, CdSe QDs were titrated with TMA and the outcome was followed by UV–vis absorption and solution ^{1}H NMR, as summarized in **Figure 4**.

The colloidal stability is clearly preserved up to 25 molecules of TMA per QD (i.e. around 30% of the original oleate molecules on the surface) with no band shifting, but the QDs start to lose colloidal stability for larger amounts of TMA (**Figure S6**).

Figure 4a shows that the first excitonic peak of the absorption spectra remain in the same position up to 25 TMA molecules with only a small broadening of the excitonic band, while for greater additions of TMA the band significantly red-shifts and broadens, which is a clear indication of sample aggregation, consistent with the observed loss of colloidal stability.

In the ^{1}H NMR spectrum of as-synthesized CdSe QDs (**Figure S3**), the alkene resonance of OLAC at 5.7 ppm is well separated from other resonances and provides a diagnostic tool to track the fate of the ligands through the titration. The QD–ligand interaction results in a significant line-broadening and shift of the alkene ^{1}H resonance towards higher frequency in the as-synthesized QDs compared to free OLAC (**Figure 4b**).[77]

The chemical shift of the alkene resonance is progressively displaced towards lower frequency as TMA is titrated into the QDs solution. Above 25 TMA molecules, when the QDs lose colloidal stability, the alkene resonance sharpens significantly. Nevertheless, the peak remains broad enough to obscure the J-coupling pattern of the free OLAC alkene resonances. A similar signal is seen in the ^{1}H NMR of a (1:1) mixture of TMA and OLAC (**Figure S7**). This result suggests that a variety of multinuclear TMA–OLAC complexes form (**Figure S7** and **Figure S8**). The coordination of an oleate to multiple aluminum atoms causes its desorption from the QD surface, which therefore precipitates.

Altogether, these data indicate that the TMA does interact with the oleate ligands to the point that their chemical affinity towards the surface is finally modified.

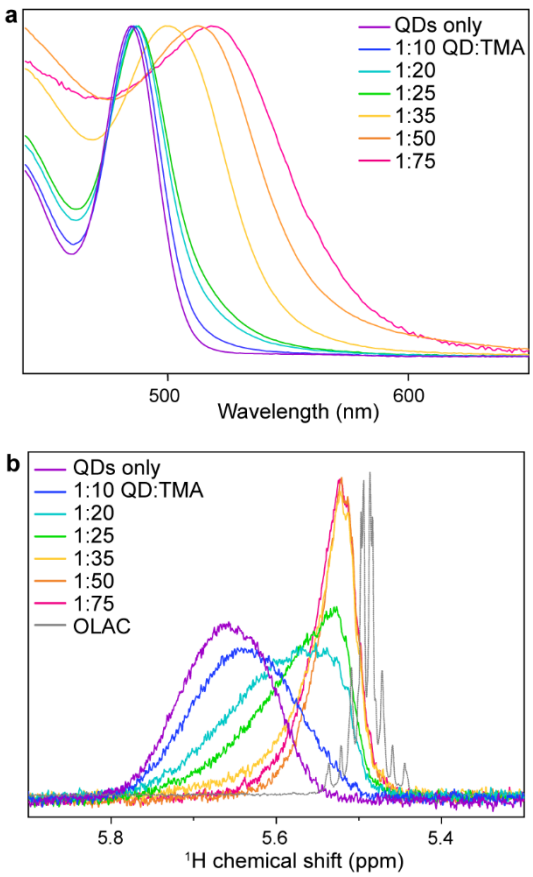

Figure 4. (a) Normalized UV–vis absorption spectra of the first excitonic peak of the TMA titrated CdSe QDs. (b) Alkene region of the ^{1}H NMR spectra for CdSe QDs titrated with increasing amounts of TMA in toluene-d_8. The labels indicate the number of TMA molecules per QD.

Structural insight via solid state NMR

In order to determine the interaction between the TMA and the ligands on the surface of CdSe QDs, DNP SENS NMR experiments were performed.

Cadmium NMR can be used to probe the inorganic core of the QDs; cadmium has two NMR active isotopes, ^{111}Cd and ^{113}Cd, with similar natural abundances (~12%) and Larmor frequencies (84.8 MHz and 88.8 MHz at 9.4 T), although ^{113}Cd has a slightly higher sensitivity.^{1}H→^{113}Cd cross polarization (CP) transfers magnetization from ^{1}H nuclei in the ligands to ^{113}Cd nuclei at and near the surface of the QD, resulting in a surface-selective spectrum. Hyperpolarization of the ^{1}H nuclei by DNP affords a signal enhancement in the ^{113}Cd spectrum, here by a factor of 33 for the as-synthesized CdSe QDs, and therefore high sensitivity (**Figure S9a**); however, due to the combination of multiple broad resonances with reasonably large chemical shift anisotropies (CSAs), the 1D ^{113}Cd spectrum is largely unresolved at the

moderate MAS rate of 8 kHz. Consequently, 2D phase-adjusted spinning sidebands (PASS) spectra were measured, which yield a resolved sideband-free spectrum in the direct dimension (*x* axis) and show the CSA for each site in the indirect dimension (*y* axis).[51,78] **Figure 5** reports the DNP-enhanced $^{1}H \rightarrow ^{113}Cd$ CP-PASS spectra of pristine CdSe QDs and CdSe@$AlO_{x(n=1)}$, with the extracted chemical shift parameters given in **Table S2**. The signal at −50 ppm with a small CSA corresponds to the symmetric ^{113}Cd site in the core of the CdSe QDs.[36,50,54] The more anisotropic signals at −320 and −440 ppm correspond to chelating $CdSe_2O_2$ and bridging-tilting $CdSeO_3$ surface sites on {100} and {111} facets, respectively, according to recently reported calculations;[54] the greater CSA arises from the lowering of symmetry at the surface. The narrow signal at −630 ppm has been previously attributed to isolated Cd(oleate)$_2$ impurities.[52]

The CdSe@$AlO_{x(n=1)}$ sample exhibits a DNP enhancement of a factor 50 (**Figure S9b**). The alumina deposition with 25 molecules of TMA prompts the appearance of two new ^{113}Cd signals located at −140 and −600 ppm. The former can be identified as surface $CdSe_3O$ species, which can be found in bridging configurations for {111} facets.[54] In contrast, the signal at -−600 ppm corresponds to a new Cd environment that we attribute to the proximity of the newly added AlO_x to Cd surface sites. This assignment is corroborated by the $^{111}Cd\{^{27}Al\}$ resonance echo saturation pulse double resonance (RESPDOR)[79] spectrum (**Figure S10**) which shows dephasing of ^{111}Cd signal near ca. −500 ppm, indicating that these environments are proximal to ^{27}Al. For the CdSe@$AlO_{x(n=3)}$ sample (**Figure S11** and **Table S2**), a similar ^{113}Cd spectrum is observed, but with a greater relative proportion of the new signal at −600 ppm, and slightly less of the major −320 ppm signal (**Figure 5c**). This suggests that after one c-ALD cycle, not all the QD surface has been functionalized with the deposited alumina and that there can still be available QD surface regions to interact with on the following cycles.

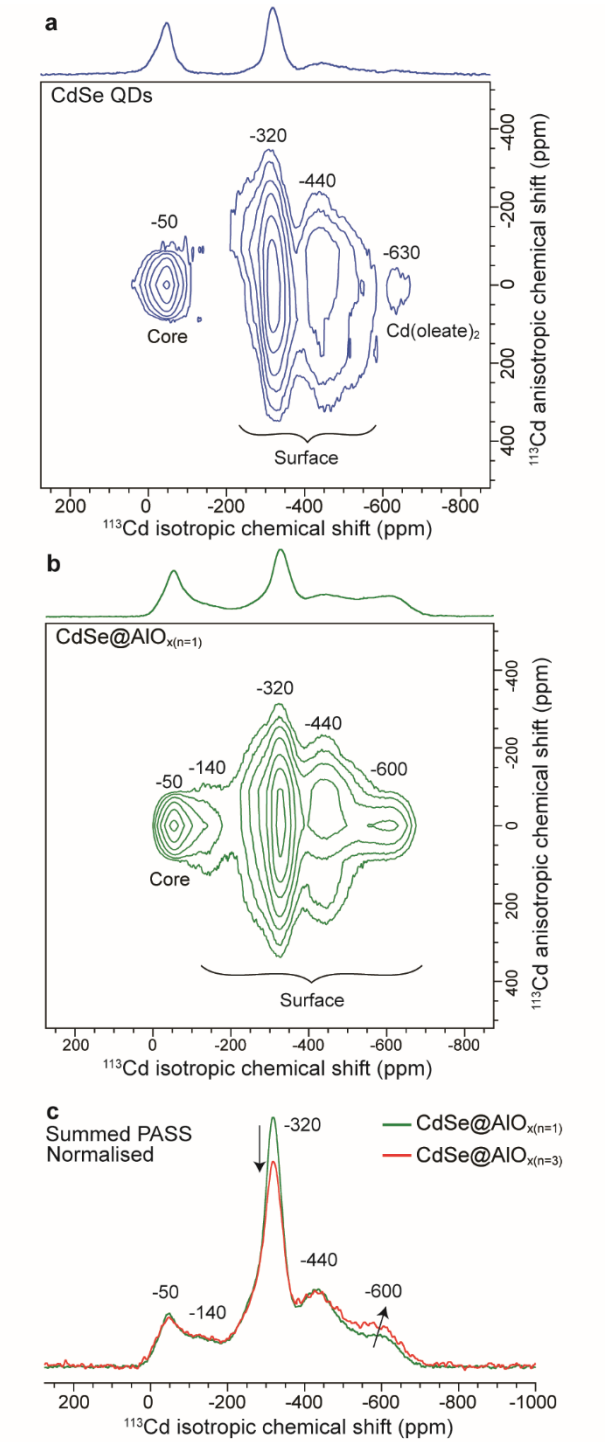

Figure 5. DNP-enhanced $^{1}H \rightarrow ^{113}Cd$ CP-PASS spectra of (a) CdSe QDs and (b) $CdSe@AlO_{x(n=1)}$, labelled with the isotropic chemical shifts. The CSA parameters are given in **Table S2**. (c) Comparison of the isotropic ^{113}Cd spectra obtained by summation of the slices in the PASS spectra for 1 and 3 cycles of c-ALD, normalized to the core signal at −50 ppm.

The inorganic and organic components of the hybrid shell can also be probed individually using ^{27}Al and ^{13}C NMR, respectively. The formation of the AlO_x shell is evident from the DNP-

enhanced $^{1}H \rightarrow ^{27}Al$ CP spectra shown in **Figure 6a**. Here, three signals are observed which correspond to aluminum oxide environments with 4-, 5-, and 6-fold coordination by oxygen.[80] There is a greater relative proportion of octahedrally coordinated Al(6) after three c-ALD cycles (n = 3) compared to n = 1, consistent with a thicker shell, which contains more bulk like (octahedrally coordinated) alumina.

The DNP-enhanced $^{1}H \rightarrow ^{13}C$ CP spectra of CdSe QDs (**Figure 6b**) reveal the typical signals for oleate ligands. The broader signals covering the range from 20–40 ppm correspond to carbons of the alkyl chain and the signal at 15 ppm is attributed to the methyl terminating moiety of the oleate ligands. The intense signal at 74 ppm corresponds to TCE from the DNP sample preparation. The signals at 130 and 184 ppm are attributed to the alkene and carboxylate carbons of the oleate ligands respectively. The chemical shifts of most of the signals are not affected by the deposition of an alumina layer; however, a clear shift and shoulder can be observed for the carboxylate signal (**Figure 6b** and deconvolution in **Figure S12**). Consistently with the FTIR results (see above), the low-frequency asymmetry in the carboxylate signal can be ascribed to a contribution of ligands in a bridging coordinating mode.[73]

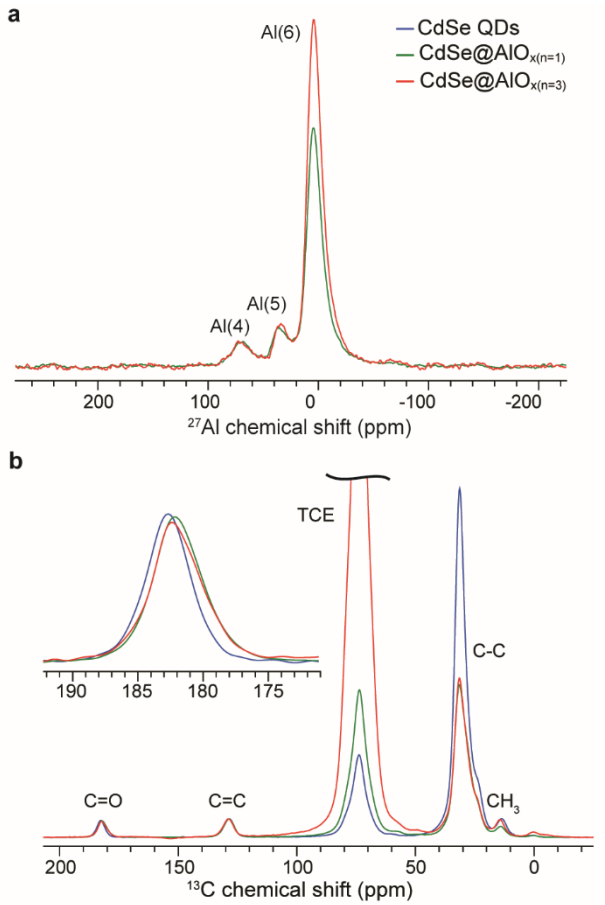

Figure 6. (a) $^{1}H \rightarrow ^{27}Al$ CP spectra of CdSe QDs with one and three cycles of alumina deposition, normalized to the same Al(4) intensity for comparison. (b) $^{1}H \rightarrow ^{13}C$ CP spectra of

as-synthesized CdSe QDs and CdSe QDs with one and three cycles of alumina deposition, normalized to the alkene intensity. The larger relative intensity of the alkyl ^{13}C signal for the pristine sample is ascribed to differences in dynamics between the samples.

To interrogate the local bonding between the inorganic AlO_x shell and the organic ligands at the surface of the QDs, we performed $^{13}C\{^{27}Al\}$ RESPDOR experiments on CdSe@$AlO_{x(n=1)}$, which are enabled by the high sensitivity afforded by DNP. In a RESPDOR experiment, a ^{13}C spin echo is performed while recoupling heteronuclear (i.e. ^{13}C–^{27}Al) dipolar interactions; if the ^{27}Al spins are saturated half way through the echo, the ^{13}C–^{27}Al coupling is not refocused, resulting in a decay for the signals of any ^{13}C spins that are near ^{27}Al (**Figure S13**). In the ^{13}C RESPDOR spectra of CdSe@$AlO_{x(n=1)}$ (**Figure 7a**), a clear dephasing on the carboxylate carbon of the native ligands is observed, indicating that this is the moiety in atomic-proximity to Al atoms. In contrast, the rest of the oleate signals do not exhibit dephasing, as after one cycle of c-ALD the AlO_x shell does not extend towards the ligand tails.

Varying the recoupling time in the RESPDOR experiment yields a dephasing curve which allows the ^{13}C–^{27}Al dipolar coupling to be quantified and the ^{13}C–^{27}Al distance calculated. **Figure 7b** plots the $^{13}C\{^{27}Al\}$ RESPDOR dephasing curve obtained up to 3 ms recoupling time. The curve was fitted with a previously described analytical expression[81] (see Supporting Information for details) that results in an average ^{13}C–^{27}Al dipolar coupling of 503 Hz, corresponding to a ^{13}C–^{27}Al distance for the carboxylate carbon of 2.5 Å. The fitted pre-factor of $f = 0.24$ indicates that approximately a quarter of the ligands are bonded to Al (assuming the ^{27}Al is fully saturated), consistent with the ratio of the 25 TMA molecules added and the expected coverage of 85–90 ligands per QD. In summary, the short distance determined from the RESPDOR dephasing indicates that there must be direct bonding between Al and the carboxylate group of the ligand.

Having established the C–Al distance by NMR, the structure of the complex was investigated via DFT structure calculations for an oleate passivated CdSe {100} surface, directly after reaction with a TMA molecule and an O_2 molecule. In the simplest case, with only one chelating ligand present at the surface (**Figure 7c**, **Figure S14**), a ^{13}C–^{27}Al distance of 2.9 Å was observed. Calculations were also performed in more complex scenarios, where ligands are present on the surface with a density closer to the experimentally measured one (**Figure 7d**, **Figure S14**). In such cases, a shorter distance of 2.8 Å was found. These distances are in fair agreement with the RESPDOR results. Some discrepancy between the NMR and DFT distances may arise from some ligands being near to multiple ^{27}Al ions, leading to greater

dephasing and an overestimation of the ^{13}C–^{27}Al dipolar coupling. Interestingly, during the relaxation of one of the structures including additional ligands, the originally chelating ligands modify their binding mode to be more bridging-like (**Figure 7d**). This computational result concurs with the FTIR and ^{13}C NMR characterization showing that the coordination configuration of ligands presents features from chelating as well as bridging upon alumina deposition by c-ALD.

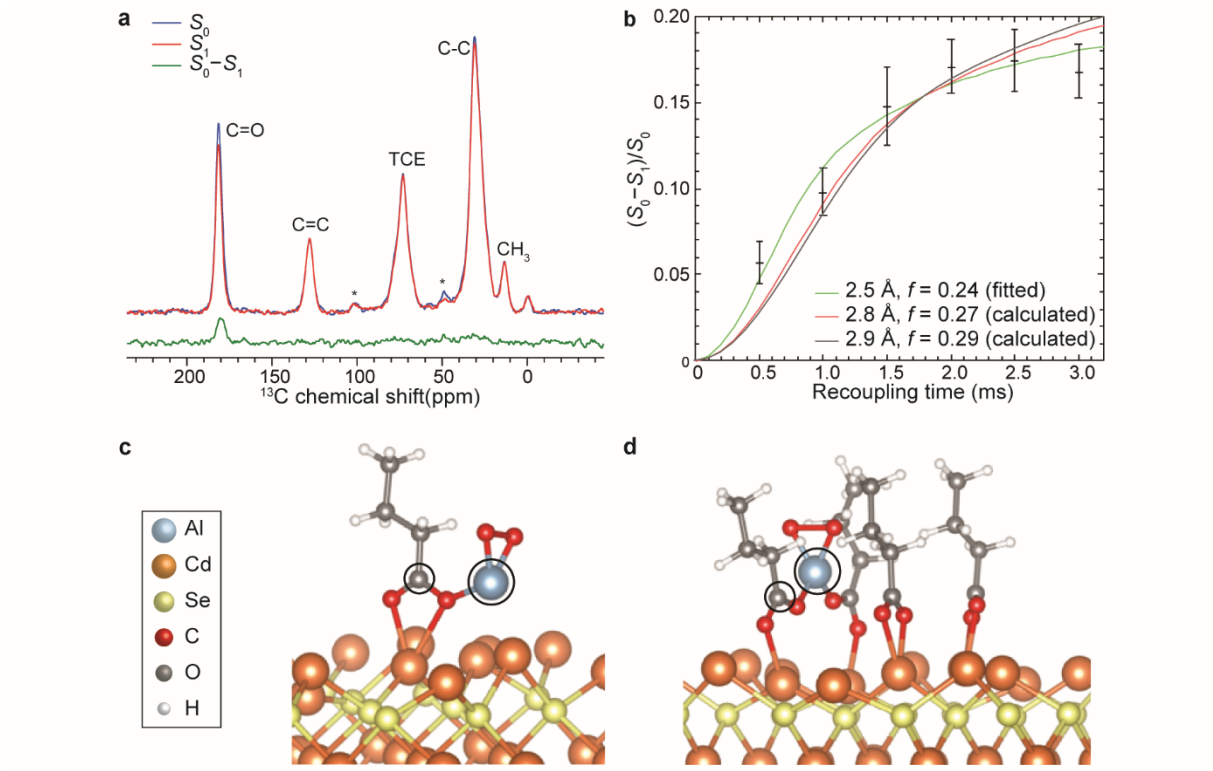

Figure 7. (a) $^{13}C\{^{27}Al\}$ RESPDOR spectrum with 3 ms of REDOR recoupling, with (S_1) and without (S_0) ^{27}Al saturation. The difference spectrum (S_0 – S_1) shows dephasing of the carboxylate carbon signal. Asterisks indicate spinning sidebands. (b) Dephasing curve for the carboxylate signal with simulated curves using a previously described analytical expression for different ^{27}Al–^{13}C distances (see Supporting Information for additional details).[81] (c,d) Schematics of the ligand–TMA complex on the CdSe {100} surface from DFT structural calculations considering (c) one ligand and (d) four ligands on the surface. The black circles indicating the carbon and aluminum atoms probed in the recoupling experiment.

CONCLUSION

We have determined the mechanism, and the vital role of the ligands, for AlO_x deposition on oleate-capped CdSe QDs to form CdSe@AlOx hybrids by c-ALD. ^{1}H solution NMR confirmed the interaction of the native oleate ligands with the TMA precursor, and FTIR and XPS analysis provided insight into the surface chemistry changes caused by the shell deposition. Finally, DNP SENS recoupling experiments and DFT structure calculations proved that TMA reacts with the oxygen-containing carboxylate moiety and remains attached to the QD surface. This new knowledge highlights that the organic ligands on the surface of colloidal NPs are the keystone for the nucleation of the metal-oxide shell in c-ALD via the formation of a ligand-precursor complex.

Having learned this, precursors for the oxide matrix can be selected to specifically react with the NP surface ligands. The c-ALD chemistry can then be further exploited towards the synthesis of multifunctional organic–inorganic hybrid materials where the two components can be modified to tailor the desired properties. For example, the presence of the organic component in the inorganic network could be used to add photoactive moieties, or alternatively, removal of the organic species via annealing might be considered to create controlled porosity.

ASSOCIATED CONTENT

The Supporting Information is available and free of charge and contains additional experimental details, computational methods and calculations, UV-vis and PL emission spectra, TEM micrographs, ^{1}H NMR, DOSY decay fittings, additional XPS details, additional solid-state NMR details and discussions.

ACKNOWLEDGMENTS

This work was primarily financed by NCCR Catalysis, a National Centre of Competence in Research funded by the Swiss National Science Foundation. M.A.H., A.V. and K.R. acknowledge H2020 Marie Skłodowska-Curie Individual fellowships with grant numbers 101024144, 101024369 and 890414, respectively. The theoretical effort was supported by EPFL computational facilities and the Swiss National Supercomputer Center (CSCS), project "sm54". L.E. is grateful for financial support from the Swiss National Science Foundation, grant number 200020_178860. The authors thank Petru Albertini for helpful discussions on the deposition mechanisms of the alumina shell.

EXPERIMENTAL SECTION

Chemicals. Cadmium nitrate tetrahydrate ($Cd(NO_3)_2 \cdot 4H_2O$, ≥99%), selenium powder (99.99%), myristic acid (98%), oleic acid (OLAC, 90% technical grade), ethanol (EtOH, anhydrous, 95%), hexagonal boron nitride (h-BN, 98%) and octane (anhydrous, ≥99%) were purchased from Sigma-Aldrich. Octadecene (ODE, 90% technical grade), toluene-d8 (Tol-d_8, 99.5 atom % D), 1,1,2,2-tetrachloroethane (TCE, 99%) and dibromomethane (CH_2Br_2, 99%) were purchased from Acros. Hexane (anhydrous, >96%) was purchased from TCI. Trimethylaluminum (TMA, 98%) was purchased from Strem. The TEKPol biradical was provided by Dr. Olivier Ouari (Aix Marseille University).

Materials synthesis. All procedures are performed connected to a standard N_2 (g) Schlenk line.

Cd(myristate)$_2$. $Cd(myr)_2$ was synthesized by adapting a protocol from Knittel and co-workers.[58] Myristic acid (6.85 g, 30 mmol) and $Cd(NO_3)_2 \cdot 4H_2O$ (4.62 g, 15 mmol) were dissolved in 650 mL of MeOH under magnetic stirring. 1.81 g (45 mmol) of NaOH in 50 mL MeOH were added dropwise with a dropping funnel, followed by vigorous stirring for 30 minutes. $Cd(myr)_2$ precipitated as a white, fluffy solid. The product was filtered, washed three times with MeOH and dried overnight under vacuum.

CdSe quantum dots. CdSe QDs were synthesized by adapting a protocol from Knittel and co-workers. A mixture of 96 mL of ODE, $Cd(myr)_2$ (1.022 g, 1.8 mmol) and Se (0.072 g, 0.9 mmol) was degassed at room temperature for 30 min in a 250 mL three-neck round-bottom flask. The solution was heated to 240 °C under N_2 in a few minutes without overshooting. Oleic acid (3 mL, 9.5 mmol) was injected after 5 minutes of reaction before the heating mantle was removed to quench the reaction. The nanocrystals were then washed by six cycles of precipitation with ethanol and redispersion in hexane (EtOH:hexane 1:1, 13500 rpm, 20 min).

Sample preparation for ^{1}H NMR titrations. The concentration of the CdSe QD stock solution was determined from the first excitonic transition absorbance according to previous reports (see Supporting Information for further details).[59] 120 μM samples of QDs were prepared from the stock solution in 0.4 mL toluene-d8. Increasing volumes of a stock solution of TMA in toluene-d_8 (6.5 mM) were titrated into the CdSe QDs samples. Additional toluene-d_8 was added to ensure all aliquots had a final 50 μM concentration.

AlO_x shell deposition. A diluted solution of CdSe QDs in octane (3 μM) was stirred in a three-necked flask under N_2 flow. One c-ALD cycle consists of (1) dropwise addition of a 1.6mM TMA solution (volume corresponding to 25 TMA molecules per QD) to the reaction flask at 1

mL/h and (2) addition of O_2 (in excess at 1.5 mL/min) by means of a mass flow controller. Both steps are followed by 5 min waiting time to ensure half-reactions are completed.

For controlled additions of TMA, a SGE gas tight syringe (5 mL) with a removable stainless steel Luer-lock needle (22 gauge, 12 inches) was used combined with a Chemyx Fusion 200 two-channel injection pump.

Characterization. UV–vis absorption measurements were performed in a Perkin Elmer Lambda 950 Spectrophotometer equipped with deuterium and tungsten halide light sources and a photomultiplier tube with Peltier-controlled PbS detector. Colloidal suspensions of QDs in hexane were measured in quartz cuvettes.

XPS measurements were recorded using a Kratos Analytical instrument, using the monochromatic Kα X-ray line of an Al anode. The pass energy was set to 20 eV with a step size of 0.1 eV. The samples were prepared by drop-casting nanocrystal films onto clean Si substrates. The samples were electrically insulated from the sample holder and charges were compensated. Curve fitting was performed using the CasaXPS software. Spectra were referenced at 284.8 eV using the C-C bond of the C1s orbital.

FTIR measurements were carried out on an attenuated total reflectance (ATR) PerkinElmer Two spectrometer. Samples dispersed in hexane were directly deposited by drop-casting on the ATR plate after measuring the background with air. The resolution used to acquire the spectra was 4 cm^{-1}.

HAADF-STEM imaging and energy dispersive X-ray analysis (EDX) were performed on a FEI Tecnai Osiris TEM in scanning mode at an accelerating voltage of 200 kV. This microscope is equipped with a high brightness X-FEG gun, silicon drift Super-X EDX detector and a Bruker Esprit acquisition software. Samples were drop-casted on a gold TEM grid (Ted Pella, Inc.) prior to imaging.

Solution NMR measurements were recorded on a Bruker Avance III HD 400 MHz 9.4 T spectrometer equipped with a BBFO liquid probe. One dimensional (1D) ^1H and 2D DOSY spectra were acquired using a standard pulse sequence from the Bruker library.

DNP experimental details. DNP-enhanced solid-state NMR spectra were acquired at 100 K on a 9.4 T Bruker AVANCE III spectrometer, corresponding to a ^1H Larmor frequency of 400 MHz, using a 263 GHz gyrotron microwave source and a low-temperature MAS probe for 3.2 mm outer-diameter rotors. QDs were precipitated by the addition of an antisolvent (EtOH) and physically mixed with hexagonal boron nitride to disperse the QDs and maximize microwave penetration,[52,82] followed by impregnation with a 16 mM solution of the TEKPol biradical in

degassed 1,1,2,2-tetracholoethane (TCE).[83] The samples were prepared and packed into sapphire rotors in a nitrogen glovebox. ^{13}C spectra were recorded by taking the isotropic slice of a CP PASS experiment, ^{27}Al spectra used an echo-detected CP experiment, and ^{113}Cd spectra were obtained using CP PASS or CP Carr–Purcell–Meiboom–Gill (CPMG) experiments;[84] see **Table S3** for details. RESPDOR experiments were performed with the pulse sequences shown in **Figure S13**.[79,81] $^{111}Cd\{^{27}Al\}$ experiments were performed using adiabatic $SR4_1^2$ recoupling,[85–87] CPMG acquisition,[88] and a triple resonance probe configuration. $^{13}C\{^{27}Al\}$ experiments were performed using REDOR recoupling[89] (i.e. a train of π pulses applied every half rotor period), in a double mode configuration with the tuning split by a REDOR box (NMR Service GmbH) (**Figure S13**b). Further details are given in **Table S4**. ^{13}C spectra were referenced to TCE at 74 ppm at 100 K, ^{27}Al spectra to an aluminum nitrate solution at 0 ppm at room temperature, and $^{111/113}Cd$ spectra to $Cd(acac)_2$ at −596.9 ppm at 100 K (relative to dimethyl cadmium as the primary reference). Spectral deconvolution was performed with the dmfit software,[90] and CPMG spectra were processed to give the conventional spectra by summing the echoes before Fourier transformation using the RMN 2.0 software (PhySy Ltd.).

REFERENCES

(1) Sanchez, C.; Belleville, P.; Popall, M.; Nicole, L. Applications of Advanced Hybrid Organic-Inorganic Nanomaterials: From Laboratory to Market. *Chem. Soc. Rev.* **2011**, *40* (2), 696–753.

(2) Vallet-Regí, M.; Colilla, M.; González, B. Medical Applications of Organic–Inorganic Hybrid Materials within the Field of Silica-Based Bioceramics. *Chem. Soc. Rev.* **2011**, *40* (2), 596–607.

(3) Nicole, L.; Laberty-Robert, C.; Rozes, L.; Sanchez, C. Hybrid Materials Science: A Promised Land for the Integrative Design of Multifunctional Materials. *Nanoscale* **2014**, *6* (12), 6267–6292.

(4) Brenner, T. M.; Egger, D. A.; Kronik, L.; Hodes, G.; Cahen, D. Hybrid Organic - Inorganic Perovskites: Low-Cost Semiconductors with Intriguing Charge-Transport Properties. *Nat. Rev. Mater.* **2016**, *1* (1), 1–16.

(5) Parola, S.; Julián-López, B.; Carlos, L. D.; Sanchez, C. Optical Properties of Hybrid Organic-Inorganic Materials and Their Applications. *Adv. Funct. Mater.* **2016**, *26* (36), 6506–6544.

(6) Carné, A.; Carbonell, C.; Imaz, I.; Maspoch, D. Nanoscale Metal–Organic Materials. *Chem. Soc. Rev.* **2011**, *40* (1), 291–305.

(7) Schubert, U. Cluster-Based Inorganic–Organic Hybrid Materials. *Chem. Soc. Rev.* **2011**, *40* (2), 575–582.

(8) Mirkin, C. A.; Letsinger, R. L.; Mucic, R. C.; Storhoff, J. J. A DNA-Based Method for Rationally Assembling Nanoparticles into Macroscopic Materials. *Nature* **1996**, *382*, 607–609.

(9) Pinna, N.; Garnweitner, G.; Beato, P.; Niederberger, M.; Antonietti, M. Synthesis of Yttria-Based Crystalline and Lamellar Nanostructures and Their Formation Mechanism. *Small* **2005**, *1* (1), 112–121.

(10) Karmaoui, M.; Sá Ferreira, R. A.; Mane, A. T.; Carlos, L. D.; Pinna, N. Lanthanide-Based Lamellar Nanohybrids: Synthesis, Structural Characterization, and Optical Properties. *Chem. Mater.* **2006**, *18* (18), 4493–4499.

(11) Pinna, N. The "Benzyl Alcohol Route": An Elegant Approach towards Organic-Inorganic Hybrid Nanomaterials. *J. Mater. Chem.* **2007**, *17* (27), 2769–2774.

(12) Cao, M.; Djerdj, I.; Jagličić, Z.; Antonietti, M.; Niederberger, M. Layered Hybrid Organic-Inorganic Nanobelts Exhibiting a Field-Induced Magnetic Transition. *Phys. Chem. Chem. Phys.* **2009**, *11* (29), 6166–6172.

(13) Djerdj, I.; Cao, M.; Rocquefelte, X.; Černý, R.; Jagličić, Z.; Arčon, D.; Potočnik, A.; Gozzo, F.; Niederberger, M. Structural Characterization of a Nanocrystalline Inorganic-Organic Hybrid with Fiberlike Morphology and One-Dimensional Antiferromagnetic Properties. *Chem. Mater.* **2009**, *21* (14), 3356–3369.

(14) Baek, W.; Bootharaju, M. S.; Walsh, K. M.; Lee, S.; Gamelin, D. R.; Hyeon, T. Highly Luminescent and Catalytically Active Suprastructures of Magic-Sized Semiconductor Nanoclusters. *Nat. Mater.* **2021**, *20* (5), 650–657.

(15) Direj, S.; Babonneau, F.; Sanchez, C.; Livage, J. Sol-Gel Synthesis of Siloxane-Oxide Hybrid Coatings [$Si(CH_3)_2O{\cdot}MO_x$: M = Si, Ti, Zr, Al] with Luminescent Properties. *J. Mater. Chem.* **1992**, *2* (2), 239–244.

(16) Schaudel, B.; Guermeur, C.; Sanchez, C.; Nakatani, K.; Delaire, J. A. Spirooxazine- and Spiropyran-Doped Hybrid Organic-Inorganic Matrices with Very Fast Photochromic Responses. *J. Mater. Chem.* **1997**, *7* (1), 61–65.

(17) Sanchez, C.; Ribot, F.; Lebeau, B. Molecular Design of Hybrid Organic-Inorganic Nanocomposites Synthesized via Sol-Gel Chemistry. *J. Mater. Chem.* **1999**, *9* (1), 35–44.

(18) Mishra, S.; Daniele, S. Molecular Engineering of Metal Alkoxides for Solution Phase Synthesis of High-Tech Metal Oxide Nanomaterials. *Chem. Eur. J.* **2020**, *26* (42), 9292–

9303.

(19) Loiudice, A.; Strach, M.; Saris, S.; Chernyshov, D.; Buonsanti, R. Universal Oxide Shell Growth Enables in Situ Structural Studies of Perovskite Nanocrystals during the Anion Exchange Reaction. *J. Am. Chem. Soc.* **2020**, *141* (20), 8254–8263.

(20) Loiudice, A.; Saris, S.; Buonsanti, R. Tunable Metal Oxide Shell as a Spacer to Study Energy Transfer in Semiconductor Nanocrystals. *J. Phys. Chem. Lett.* **2020**, *11* (9), 3430–3435.

(21) Loiudice, A.; Segura Lecina, O.; Bornet, A.; Luther, J. M.; Buonsanti, R. Ligand Locking on Quantum Dot Surfaces via a Mild Reactive Surface Treatment. *J. Am. Chem. Soc.* **2021**, *143* (33), 13418–13427.

(22) Sachleben, J. R.; Wooten, E. W.; Emsley, L.; Pines, A.; Colvin, V. L.; Alivisatos, A. P. NMR Studies of the Surface Structure and Dynamics of Semiconductor Nanocrystals. *Chem. Phys. Lett.* **1992**, *198* (5), 431–436.

(23) Sachleben, J. R.; Colvin, V.; Emsley, L.; Wooten, E. W.; Alivisatos, A. P. Solution-State NMR Studies of the Surface Structure and Dynamics of Semiconductor Nanocrystals. *J. Phys. Chem. B* **1998**, *102* (50), 10117–10128.

(24) Fritzinger, B.; Moreels, I.; Lommens, P.; Koole, R.; Hens, Z.; Martins, J. C. In Situ Observation of Rapid Ligand Exchange in Colloidal Nanocrystal Suspensions Using Transfer NOE Nuclear Magnetic Resonance Spectroscopy. *J. Am. Chem. Soc.* **2009**, *131* (8), 3024–3032.

(25) Fritzinger, B.; Capek, R. K.; Lambert, K.; Martins, J. C.; Hens, Z. Utilizing Self-Exchange to Address the Binding of Carboxylic Acid Ligands to CdSe Quantum Dots. *J. Am. Chem. Soc.* **2010**, *132* (29), 10195–10201.

(26) Hens, Z.; Martins, J. C. A Solution NMR Toolbox for Characterizing the Surface Chemistry of Colloidal Nanocrystals. *Chem. Mater.* **2013**, *25* (8), 1211–1221.

(27) Anderson, N. C.; Owen, J. S. Soluble, Chloride-Terminated CdSe Nanocrystals: Ligand Exchange Monitored by ^{1}H and ^{31}P NMR Spectroscopy. *Chem. Mater.* **2013**, *25* (1), 69–76.

(28) Marbella, L. E.; Millstone, J. E. NMR Techniques for Noble Metal Nanoparticles. *Chem. Mater.* **2015**, *27* (8), 2721–2739.

(29) De Roo, J.; Ibáñez, M.; Geiregat, P.; Nedelcu, G.; Walravens, W.; Maes, J.; Martins, J. C.; Van Driessche, I.; Kovalenko, M. V.; Hens, Z. Highly Dynamic Ligand Binding and Light Absorption Coefficient of Cesium Lead Bromide Perovskite Nanocrystals. *ACS Nano* **2016**, *10* (2), 2071–2081.

(30) Drijvers, E.; De Roo, J.; Martins, J. C.; Infante, I.; Hens, Z. Ligand Displacement Exposes Binding Site Heterogeneity on CdSe Nanocrystal Surfaces. *Chem. Mater.* **2018**, *30* (3), 1178–1186.

(31) Casabianca, L. B. Solid-State Nuclear Magnetic Resonance Studies of Nanoparticles. *Solid State Nucl. Magn. Reson.* **2020**, *107*, 101664.

(32) Marchetti, A.; Chen, J.; Pang, Z.; Li, S.; Ling, D.; Deng, F.; Kong, X. Understanding Surface and Interfacial Chemistry in Functional Nanomaterials via Solid-State NMR. *Adv. Mater.* **2017**, *29*, 1605895.

(33) Kaushik, M.; Leroy, C.; Chen, Z.; Gajan, D.; Willinger, E.; Müller, C. R.; Fayon, F.; Massiot, D.; Fedorov, A.; Copéret, C.; Lesage, A.; Florian, P. Atomic-Scale Structure and Its Impact on Chemical Properties of Aluminum Oxide Layers Prepared by Atomic Layer Deposition on Silica. *Chem. Mater.* **2021**, *33* (9), 3335–3348.

(34) Becerra, L. R.; Murray, C. B.; Griffin, R. G.; Bawendi, M. G. Investigation of the Surface Morphology of Capped CdSe Nanocrystallites by ^{31}P Nuclear Magnetic Resonance. *J. Chem. Phys.* **1994**, *100* (4), 3297–3300.

(35) Ladizhansky, V.; Hodes, G.; Vega, S. Surface Properties of Precipitated CdS Nanoparticles Studied by NMR. *J. Phys. Chem. B* **1998**, *102* (43), 8505–8509.

(36) Ratcliffe, C. I.; Yu, K.; Ripmeester, J. A.; Badruz Zaman, M.; Badarau, C.; Singh, S. Solid State NMR Studies of Photoluminescent Cadmium Chalcogenide Nanoparticles. *Phys. Chem. Chem. Phys.* **2006**, *8* (30), 3510–3519.

(37) Badia, A.; Gao, W.; Singh, S.; Demers, L.; Cuccia, L.; Reven, L. Structure and Chain Dynamics of Alkanethiol-Capped Gold Colloids. *Langmuir* **1996**, *12* (5), 1262–1269.

(38) Al-Johani, H.; Abou-Hamad, E.; Jedidi, A.; Widdifield, C. M.; Viger-Gravel, J.; Sangaru, S. S.; Gajan, D.; Anjum, D. H.; Ould-Chikh, S.; Hedhili, M. N.; Gurinov, A.; Kelly, M. J.; Eter, M. El; Cavallo, L.; Emsley, L.; Basset, J. M. The Structure and Binding Mode of Citrate in the Stabilization of Gold Nanoparticles. *Nat. Chem.* **2017**, *9* (9), 890–895.

(39) Cros-Gagneux, A.; Delpech, F.; Nayral, C.; Cornejo, A.; Coppel, Y.; Chaudret, B. Surface Chemistry of InP Quantum Dots: A Comprehensive Study. *J. Am. Chem. Soc.* **2010**, *132* (51), 18147–18157.

(40) Chen, Y.; Smock, S. R.; Flintgruber, A. H.; Perras, F. A.; Brutchey, R. L.; Rossini, A. J. Surface Termination of $CsPbBr_3$ Perovskite Quantum Dots Determined by Solid-State NMR Spectroscopy. *J. Am. Chem. Soc.* **2020**, *142* (13), 6117–6127.

(41) Alam, K. M.; Jensen, C. E.; Kumar, P.; Hooper, R. W.; Bernard, G. M.; Patidar, A.;

Manuel, A. P.; Amer, N.; Palmgren, A.; Purschke, D. N.; Chaulagain, N.; Garcia, J.; Kirwin, P. S.; Shoute, L. C. T.; Cui, K.; Gusarov, S.; Kobryn, A. E.; Michaelis, V. K.; Hegmann, F. A.; Shankar, K. Photocatalytic Mechanism Control and Study of Carrier Dynamics in CdS@C_3N_5 Core–Shell Nanowires. *ACS Appl. Mater. Interfaces* **2021**, *13* (40), 47418–47439.

(42) Lesage, A.; Lelli, M.; Gajan, D.; Caporini, M. A.; Vitzthum, V.; Miéville, P.; Alauzun, J.; Roussey, A.; Thieuleux, C.; Mehdi, A.; Bodenhausen, G.; Copéret, C.; Emsley, L. Dynamic Nuclear Polarization Surface Enhanced NMR Spectroscopy. *J. Am. Chem. Soc.* **2010**, *132*, 15459–15461.

(43) Lelli, M.; Gajan, D.; Lesage, A.; Caporini, M. A.; Vitzthum, V.; Miéville, P.; Héroguel, F.; Rascón, F.; Roussey, A.; Thieuleux, C.; Boualleg, M.; Veyre, L.; Bodenhausen, G.; Copéret, C.; Emsley, L. Fast Characterization of Functionalized Silica Materials by Silicon-29 Surface-Enhanced NMR Spectroscopy Using Dynamic Nuclear Polarization. *J. Am. Chem. Soc.* **2011**, *133* (7), 2104–2107.

(44) Lafon, O.; Rosay, M.; Aussenac, F.; Lu, X.; Trébosc, J.; Cristini, O.; Kinowski, C.; Touati, N.; Vezin, H.; Amoureux, J. P. Beyond the Silica Surface by Direct Silicon-29 Dynamic Nuclear Polarization. *Angew. Chemie - Int. Ed.* **2011**, *50* (36), 8367–8370.

(45) Akbey, Ü.; Altin, B.; Linden, A.; Özçelik, S.; Gradzielski, M.; Oschkinat, H. Dynamic Nuclear Polarization of Spherical Nanoparticles. *Phys. Chem. Chem. Phys.* **2013**, *15* (47), 20706–20716.

(46) Lee, D.; Monin, G.; Duong, N. T.; Lopez, I. Z.; Bardet, M.; Mareau, V.; Gonon, L.; De Paëpe, G. Untangling the Condensation Network of Organosiloxanes on Nanoparticles Using 2D 29Si-29Si Solid-State NMR Enhanced by Dynamic Nuclear Polarization. *J. Am. Chem. Soc.* **2014**, *136* (39), 13781–13788.

(47) Rossini, A. J.; Zagdoun, A.; Lelli, M.; Lesage, A.; Copéret, C.; Emsley, L. Dynamic Nuclear Polarization Surface Enhanced NMR Spectroscopy. *Acc. Chem. Res.* **2013**, *46* (9), 1942–1951.

(48) Kobayashi, T.; Perras, F. A.; Slowing, I. I.; Sadow, A. D.; Pruski, M. Dynamic Nuclear Polarization Solid-State NMR in Heterogeneous Catalysis Research. *ACS Catal.* **2015**, *5* (12), 7055–7062.

(49) Protesescu, L.; Rossini, A. J.; Kriegner, D.; Valla, M.; De Kergommeaux, A.; Walter, M.; Kravchyk, K. V.; Nachtegaal, M.; Stangl, J.; Malaman, B.; Reiss, P.; Lesage, A.; Emsley, L.; Copéret, C.; Kovalenko, M. V. Unraveling the Core-Shell Structure of Ligand-Capped Sn/SnO_x Nanoparticles by Surface-Enhanced Nuclear Magnetic

Resonance, Mössbauer, and X-Ray Absorption Spectroscopies. *ACS Nano* **2014**, *8* (3), 2639–2648.

(50) Piveteau, L.; Ong, T. C.; Rossini, A. J.; Emsley, L.; Copéret, C.; Kovalenko, M. V. Structure of Colloidal Quantum Dots from Dynamic Nuclear Polarization Surface Enhanced NMR Spectroscopy. *J. Am. Chem. Soc.* **2015**, *137* (43), 13964–13971.

(51) Piveteau, L.; Ong, T. C.; Walder, B. J.; Dirin, D. N.; Moscheni, D.; Schneider, B.; Bär, J.; Protesescu, L.; Masciocchi, N.; Guagliardi, A.; Emsley, L.; Copéret, C.; Kovalenko, M. V. Resolving the Core and the Surface of CdSe Quantum Dots and Nanoplatelets Using Dynamic Nuclear Polarization Enhanced PASS-PIETA NMR Spectroscopy. *ACS Cent. Sci.* **2018**, *4* (9), 1113–1125.

(52) Hanrahan, M. P.; Chen, Y.; Blome-Fernández, R.; Stein, J. L.; Pach, G. F.; Adamson, M. A. S.; Neale, N. R.; Cossairt, B. M.; Vela, J.; Rossini, A. J. Probing the Surface Structure of Semiconductor Nanoparticles by DNP SENS with Dielectric Support Materials. *J. Am. Chem. Soc.* **2019**, *141* (39), 15532–15546.

(53) Piveteau, L.; Dirin, D. N.; Gordon, C. P.; Walder, B. J.; Ong, T. C.; Emsley, L.; Copéret, C.; Kovalenko, M. V. Colloidal-ALD-Grown Core/Shell CdSe/CdS Nanoplatelets as Seen by DNP Enhanced PASS-PIETA NMR Spectroscopy. *Nano Lett.* **2020**, *20* (5), 3003–3018.

(54) Chen, Y.; Dorn, R. W.; Hanrahan, M. P.; Wei, L.; Blome-Fernández, R.; Medina-Gonzalez, A. M.; Adamson, M. A. S.; Flintgruber, A. H.; Vela, J.; Rossini, A. J. Revealing the Surface Structure of CdSe Nanocrystals by Dynamic Nuclear Polarization-Enhanced ^{77}Se and ^{113}Cd Solid-State NMR Spectroscopy. *J. Am. Chem. Soc.* **2021**, *143* (23), 8747–8760.

(55) Knauf, R. R.; Lennox, J. C.; Dempsey, J. L. Quantifying Ligand Exchange Reactions at CdSe Nanocrystal Surfaces. *Chem. Mater.* **2016**, *28* (13), 4762–4770.

(56) Jasieniak, J.; Mulvaney, P. From Cd-Rich to Se-Rich - The Manipulation of CdSe Nanocrystal Surface Stoichiometry. *J. Am. Chem. Soc.* **2007**, *129* (10), 2841–2848.

(57) Lee, S. K.; Park, S. Y.; Yi, Y. S.; Moon, J. Structure and Disorder in Amorphous Alumina Thin Films: Insights from High-Resolution Solid-State NMR. *J. Phys. Chem. C* **2010**, *114* (32), 13890–13894.

(58) Knittel, F.; Gravel, E.; Cassette, E.; Pons, T.; Pillon, F.; Dubertret, B.; Doris, E. On the Characterization of the Surface Chemistry of Quantum Dots. *Nano Lett.* **2013**, *13* (11), 5075–5078.

(59) Jasieniak, J.; Smith, L.; van Embden, J.; Mulvaney, P.; Califano, M. Re-Examination of

the Size-Dependent Absorption Properties of CdSe Quantum Dots. *J. Phys. Chem. C* **2009**, *113* (45), 19468–19474.

(60) Singh, S.; Tomar, R.; Ten Brinck, S.; De Roo, J.; Geiregat, P.; Martins, J. C.; Infante, I.; Hens, Z. Colloidal CdSe Nanoplatelets, A Model for Surface Chemistry/Optoelectronic Property Relations in Semiconductor Nanocrystals. *J. Am. Chem. Soc.* **2018**, *140* (41), 13292–13300.

(61) Hassinen, A.; Moreels, I.; De Nolf, K.; Smet, P. F.; Martins, J. C.; Hens, Z. Short-Chain Alcohols Strip X-Type Ligands and Quench the Luminescence of PbSe and CdSe Quantum Dots, Acetonitrile Does Not. *J. Am. Chem. Soc.* **2012**, *134* (51), 20705–20712.

(62) Anderson, N. C.; Hendricks, M. P.; Choi, J. J.; Owen, J. S. Ligand Exchange and the Stoichiometry of Metal Chalcogenide Nanocrystals: Spectroscopic Observation of Facile Metal-Carboxylate Displacement and Binding. *J. Am. Chem. Soc.* **2013**, *135* (49), 18536–18548.

(63) Johnson, C. S. Diffusion Ordered Nuclear Magnetic Resonance Spectroscopy: Principles and Applications. *Prog. Nucl. Magn. Reson. Spectrosc.* **1999**, *34*, 203–256.

(64) Peterson, M. D.; Jensen, S. C.; Weinberg, D. J.; Weiss, E. A. Mechanisms for Adsorption of Methyl Viologen on Cds Quantum Dots. *ACS Nano* **2014**, *8* (3), 2826–2837.

(65) Shallcross, R. C.; Graham, A. L.; Karayilan, M.; Pavlopoulous, N. G.; Meise, J.; Pyun, J.; Armstrong, N. R. Influence of the Processing Environment on the Surface Composition and Electronic Structure of Size-Quantized CdSe Quantum Dots. *J. Phys. Chem. C* **2020**, *124* (39), 21305–21318.

(66) Zherebetskyy, D.; Scheele, M.; Zhang, Y.; Bronstein, N.; Thompson, C.; Britt, D.; Salmeron, M.; Alivisatos, A. P.; Wang, L.-W. Hyrdoxylation of the Surface of PbS Nanocrystals Passivated with Oleic Acid. *Science* **2014**, *344* (6190), 1380–1384.

(67) Grisorio, R.; Debellis, D.; Suranna, G. P.; Gigli, G.; Giansante, C. The Dynamic Organic/Inorganic Interface of Colloidal PbS Quantum Dots. *Angew. Chemie - Int. Ed.* **2016**, *55* (23), 6628–6633.

(68) Boles, M. A.; Ling, D.; Hyeon, T.; Talapin, D. V. Erratum: The Surface Science of Nanocrystals. *Nat. Mater.* **2016**, *15* (3), 364–364.

(69) Wei, H. H. Y.; Evans, C. M.; Swartz, B. D.; Neukirch, A. J.; Young, J.; Prezhdo, O. V.; Krauss, T. D. Colloidal Semiconductor Quantum Dots with Tunable Surface Composition. *Nano Lett.* **2012**, *12* (9), 4465–4471.

(70) Subila, K. B.; Kishore Kumar, G.; Shivaprasad, S. M.; George Thomas, K.

Luminescence Properties of CdSe Quantum Dots: Role of Crystal Structure and Surface Composition. *J. Phys. Chem. Lett.* **2013**, *4* (16), 2774–2779.

(71) Kennehan, E. R.; Munson, K. T.; Doucette, G. S.; Marshall, A. R.; Beard, M. C.; Asbury, J. B. Dynamic Ligand Surface Chemistry of Excited PbS Quantum Dots. *J. Phys. Chem. Lett.* **2020**, *11* (6), 2291–2297.

(72) Kennehan, E. R.; Munson, K. T.; Grieco, C.; Doucette, G. S.; Marshall, A. R.; Beard, M. C.; Asbury, J. B. Influence of Ligand Structure on Excited State Surface Chemistry of Lead Sulfide Quantum Dots. *J. Am. Chem. Soc.* **2021**, *143* (34), 13824–13834.

(73) Zhang, J.; Zhang, H.; Cao, W.; Pang, Z.; Li, J.; Shu, Y.; Zhu, C.; Kong, X.; Wang, L.; Peng, X. Identification of Facet-Dependent Coordination Structures of Carboxylate Ligands on CdSe Nanocrystals. *J. Am. Chem. Soc.* **2019**, *141* (39), 15675–15683.

(74) Puurunen, R. L. Surface Chemistry of Atomic Layer Deposition: A Case Study for the Trimethylaluminum/Water Process. *J. Appl. Phys.* **2005**, *97*, 121301.

(75) Richey, N. E.; De Paula, C.; Bent, S. F. Understanding Chemical and Physical Mechanisms in Atomic Layer Deposition. *J. Chem. Phys.* **2020**, *152*, 040902.

(76) Liz-Marzán, L. M.; Giersig, M.; Mulvaney, P. Synthesis of Nanosized Gold-Silica Core-Shell Particles. *Langmuir* **1996**, *12* (18), 4329–4335.

(77) De Roo, J.; Yazdani, N.; Drijvers, E.; Lauria, A.; Maes, J.; Owen, J. S.; Van Driessche, I.; Niederberger, M.; Wood, V.; Martins, J. C.; Infante, I.; Hens, Z. Probing Solvent-Ligand Interactions in Colloidal Nanocrystals by the NMR Line Broadening. *Chem. Mater.* **2018**, *30* (15), 5485–5492.

(78) Antzutkin, O. N.; Shekar, S. C.; Levitt, M. H. Two-Dimensional Sideband Separation in Magic-Angle-Spinning NMR. *J. Magn. Reson. Ser. A* **1995**, *115* (1), 7–19.

(79) Gan, Z. Measuring Multiple Carbon–Nitrogen Distances in Natural Abundant Solids Using R-RESPDOR NMR. *Chem. Commun.* **2006**, *45*, 4712–4714.

(80) MacKenzie, K. J. D.; Smith, M. E. *Multinuclear Solid-State NMR of Inorganic Materials*; Pergamon Materials Series Vol. 6; Pergamon: Amsterdam, 2002.

(81) Pourpoint, F.; Trébosc, J.; Gauvin, R. M.; Wang, Q.; Lafon, O.; Deng, F.; Amoureux, J. P. Measurement of Aluminum-Carbon Distances Using S-RESPDOR NMR Experiments. *ChemPhysChem* **2012**, *13* (16), 3605–3615.

(82) Kubicki, D. J.; Rossini, A. J.; Purea, A.; Zagdoun, A.; Ouari, O.; Tordo, P.; Engelke, F.; Lesage, A.; Emsley, L. Amplifying Dynamic Nuclear Polarization of Frozen Solutions by Incorporating Dielectric Particles. *J. Am. Chem. Soc.* **2014**, *136* (44), 15711–15718.

(83) Zagdoun, A.; Casano, G.; Ouari, O.; Schwarzwälder, M.; Rossini, A. J.; Aussenac, F.;

Yulikov, M.; Jeschke, G.; Copéret, C.; Lesage, A.; Tordo, P.; Emsley, L. Large Molecular Weight Nitroxide Biradicals Providing Efficient Dynamic Nuclear Polarization at Temperatures up to 200 K. *J. Am. Chem. Soc.* **2013**, *135* (34), 12790–12797.

(84) Siegel, R.; Nakashima, T. T.; Wasylishen, R. E. Signal-to-Noise Enhancement of NMR Spectra of Solids Using Multiple-Pulse Spin-Echo Experiments. *Concepts Magn. Reson. Part A* **2005**, *26* (2), 62–77.

(85) Brinkmann, A.; Kentgens, A. P. M. Proton-Selective ^{17}O-^{1}H Distance Measurements in Fast Magic-Angle-Spinning Solid-State NMR Spectroscopy for the Determination of Hydrogen Bond Lengths. *J. Am. Chem. Soc.* **2006**, *128* (46), 14758–14759.

(86) Chen, L.; Wang, Q.; Hu, B.; Lafon, O.; Trébosc, J.; Deng, F.; Amoureux, J. P. Measurement of Hetero-Nuclear Distances Using a Symmetry-Based Pulse Sequence in Solid-State NMR. *Phys. Chem. Chem. Phys.* **2010**, *12* (32), 9395–9405.

(87) Nagashima, H.; Trébosc, J.; Trébosc, J.; Kon, Y.; Sato, K.; Lafon, O.; Lafon, O.; Amoureux, J. P.; Amoureux, J. P.; Amoureux, J. P. Observation of Low-γ Quadrupolar Nuclei by Surface-Enhanced NMR Spectroscopy. *J. Am. Chem. Soc.* **2020**, *142* (24), 10659–10672.

(88) Larsen, F. H.; Skibsted, J.; Jakobsen, H. J.; Nielsen, N. C. Solid-State QCPMG NMR of Low-γ Quadrupolar Metal Nuclei in Natural Abundance. *J. Am. Chem. Soc.* **2000**, *122* (29), 7080–7086.

(89) Gullion, T.; Schaefer, J. Rotational-Echo Double-Resonance NMR. *J. Magn. Reson.* **2011**, *213* (2), 413–417.

(90) Massiot, D.; Fayon, F.; Capron, M.; King, I.; Le Calvé, S.; Alonso, B.; Durand, J. O.; Bujoli, B.; Gan, Z.; Hoatson, G. Modelling One- and Two-Dimensional Solid-State NMR Spectra. *Magn. Reson. Chem.* **2002**, *40* (1), 70–76.